Interpreting estimated Observation Error Statistics of Weather Radar Measurements using the ICON-LAM-KENDA System

Yuefei Zeng[1], Tijana Janjic[1], Yuxuan Feng[1,2], Ulrich Blahak[3], Alberto de Lozar[3], Elisabeth Bauernschubert[3], Klaus Stephan[3], and Jinzhong Min[2]

[1]Meteorologisches Institut, Ludwig-Maximilians-Universität (LMU) München, Munich, Germany
[2]Key Laboratory of Meteorological Disaster of Ministry of Education/Collaborative Innovation Center on Forecast and Evaluation of Meteorological Disasters, Nanjing University of Information Science & Technology, Nanjing, China
[3]Deutscher Wetterdienst, Offenbach, Germany

Correspondence: Yuxuan.Feng@physik.uni-muenchen.de

Abstract.

Assimilation of weather radar measurements including radar reflectivity and radial wind data has been operational at the Deutscher Wetterdienst, with a diagonal observation error (OE) covariance matrix. For an implementation of a full OE covariance matrix, the statistics of the OE have to be a priori estimated, for which the Desroziers method has been often used. However, the resulted statistics consists of contributions from different error sources and are difficult to interpret. In this work, we use an approach that is based on samples for truncation error in radar observation space to approximate the representation error due to unresolved scales and processes (RE) and compare its statistics with the OE statistics estimated by the Desroziers method. It is found that the statistics of the RE help the understanding of several important features in the variances and correlation length scales of the OE for both reflectivity and radial wind data and the other error sources from the microphysical scheme, radar observation operator and the superobbing technique may also contribute, for instance, to differences among different elevations and observation types. The statistics presented here can serve as a guideline for selecting which observations to assimilate and for assignment of the OE covariance matrix that can be diagonal or full and correlated.

1 Introduction

Nowadays, assimilation of weather radar measurements has been widely adopted in many weather services for convective-scale numerical weather prediction (NWP) models (Gustafsson et al., 2018). For instance, in the 3D-VAR system of the Meteo-France, Doppler radial wind measurements were first assimilated by Montmerle and Faccani (2009), and radar reflectivity measurements are assimilated by a 1D+3D-Var method (Caumont et al., 2010), which firstly derives relative humidity profiles from reflectivity data. At the Met Office, radial wind data are assimilated by the 3D-VAR (Simonin et al., 2014) and reflectivity data are assimilated through latent heat nudging (Jones et al., 2016). At the Deutscher Wetterdienst (DWD), the Kilometre-scale ENsemble Data Assimilation (KENDA) system (Schraff et al., 2016) has been developed for the the COSMO (COnsortium for Small-scale MOdelling, Baldlauf et al. 2011) and the ICON (ICOsahedral Nonhydtostatic, Zängl et al. 2015) models. Since June 2020, the radial wind and reflectivity data have been assimilated via the Local Ensemble Transform Kalman

Filter (LETKF, Hunt et al. 2007) for the COSMO-model in the operational suite; Since February 2021, the ICON-D2 is run operationally. Despite of rapid progress, convective-scale data assimilation is still at an early phase of development and a number of challenges remain for both variational and ensemble-based methods, e.g., imbalance due to rapid update (Bick et al., 2016; Lange et al., 2017; Zeng et al., 2021b), strong nonlinearity of models and observation operators (Wang and Wang, 2017), model error due to unresolved scales (Zeng et al., 2019, 2020), representation error of observations (Janjic et al., 2018), and etc. In the present work, we focus on the last topic.

As stated in Janjic et al. (2018), the observation error consists of two components in the context of data assimilation: first, the instrument error that occurs during the measurement process; second, the representation error that is understood as the difference between the actual observation and its modelled representation and it can be primarily categorized into three types: observation operator error, pre-processing or quality control error and error due to unresolved scales and processes. In this work, for brevity of text and convenience of explanation, we denote the observation error with "OE" and the instrument error with "IE", and we define the observation operator error together with pre-processing or quality control error as forward model error and denote it with "FE", and denote the representation error due to unresolved scales and processes with "RE" (i.e., OE = IE + FE + RE). In general, the FE and the RE are larger than the IE. To quantify the OE statistics, the methods of Hollingsworth and Lonnberg (1986) and Desroziers et al. (2005) has been widely used in practice. The former one is based on the first guess departure, while the latter one is based on the first guess and analysis departures and enjoys more popularity in recent years. For instance, the Met Office uses the Desroziers method to calculate the interchannel error covariances for satellites and incorporates them in the OE covariance matrix in the 3DVAR (Weston et al., 2014; Waller et al., 2016a), and so does the ECMWF (Bormann et al., 2016). The DWD specifies the OE variances for conventional observations based on the Desroziers diagnositic in the KENDA system (Schraff et al., 2016). Furthermore, the Meteo-France and Met Office have also applied the method for radial wind observations to estimate spatial error correlations that are then accounted for in the data assimilation (Wattrelot et al., 2012; Simonin et al., 2019). In the present work, we use the Desroziers method to explore characteristics of the OE for radial wind and reflectivity in the operational ICON-KENDA system of the DWD. A similar study has been done by Waller et al. (2019) but for the COSMO-KENDA system and only for the radial wind. To authors's knowledge, it is the first in-depth attempt to investigate the OE statistics (variances and correlations) of reflectivity data. However, the estimated OE statistics embraces contributions from the IE, FE and RE and it is not clear how much an individual error contributes. To approximate the RE, we assume that a high resolution model is the truth and we regard model equivalence of radar data calculated from the truth as observations (e.g., Waller et al. 2014) and evaluate the statistics from a set of samples of differences between observations and model equivalence of the low resolution model run, which can then be compared with the OE statistics estimated by the Desroziers method.

The paper is organized as follows. Section 2 describes the concepts of the two methods used here to compute the observation error statistics. Section 3 gives details about the ICON model and the radar observation operator. Section 4 presents the experimental setups and results, followed by Section 5 for summary.

2 Methodology

2.1 Samples of error due to unresolved scales and processes

In spite of increasing resolution in operational NWP models, convection can not be completely resolved and shallow convection has to be parametrized. It is known that with a higher horizontal resolution the model can better resolve updraft and vertical transportation of energy and more accurately describe orography (Wedi, 2014). To mimic the RE, one can treat the mapping of states from a high resolution model as observations (Waller et al., 2014), and the low resolution model is considered as a truncation.

Following the similar approach of Zeng et al. (2019), differences between forecasts of two model runs with different resolutions, expressed in the observation space, are used to represent the RE:

$$\boldsymbol{\eta}_k = \mathcal{H}\left(\left(\mathcal{M}^H\left(\boldsymbol{x}^H\left(t_k - t\right)\right)\right)\right) - \mathcal{H}\left(\mathcal{M}^L\left(\mathcal{T}\left(\boldsymbol{x}^H\left(t_k - t\right)\right)\right)\right), \tag{1}$$

where $\mathcal{H}$ is the observation operator, $\mathcal{M}^H$ and $\mathcal{M}^L$ are models at high and low resolutions, respectively, $\boldsymbol{x}^H$ is the state of $\mathcal{M}^H$, $\mathcal{T}$ is the interpolation operator. t is the pre-defined forecast time and t_k is an arbitrary valid time. For any t_k, we can calculate a $\boldsymbol{\eta}_k$ that is a sample for the RE A flowchart of this approach is given in Figure 2 of Zeng et al. (2019).

Running models for a period (with a certain weather pattern), a set of samples are produced. If the size of samples are sufficiently large, statistics of samples should provide useful information on the nature of the RE (under certain weather conditions). More details about the setup of model runs can be found in Section 4.1.

2.2 The Desroziers method

The Desroziers method (Desroziers et al., 2005) calculates the expected value of the outer product of the first guess departure (or called innovation) $\mathbf{d}_{o-b} = \mathbf{y^o} - \mathcal{H}(\mathbf{x}^b)$ and the analysis departure $\mathbf{d}_{o-a} = \mathbf{y^o} - \mathcal{H}(\mathbf{x}^a)$ to approximate the observation error covariance matrix:

$$\mathbf{R}_{\text{est}} = E[\mathbf{d}_{o-a}\mathbf{d}_{o-b}^{T}], \tag{2}$$

where $\mathbf{y^o}$ is the observation vector. $\mathbf{R}_{\text{est}}$ is optimal in case of a linear observation operator and uncorrelated background error and OE covariances (denoted by $\mathbf{P}^b$ and $\mathbf{R}$) that are perfectly specified. Although these assumptions are usually not satisfied in practice, $\mathbf{R}_{\text{est}}$ is still widely used as a qualitative indicator for the OE statistics. Besides, Desroziers et al. (2005) initially suggested applying Eq. 2 in successive iterations to converge the truth, however, a useful estimation can be often obtained in the first iteration Waller et al. (2016b). Therefore, considering the computational cost, most of studies with operational NWP models have performed only the first iteration (e.g., Weston et al. 2014; Lange and Janjić 2016; Waller et al. 2016a; Bormann et al. 2016). In this work, we also compute the Desroziers diagnostic in one iteration.
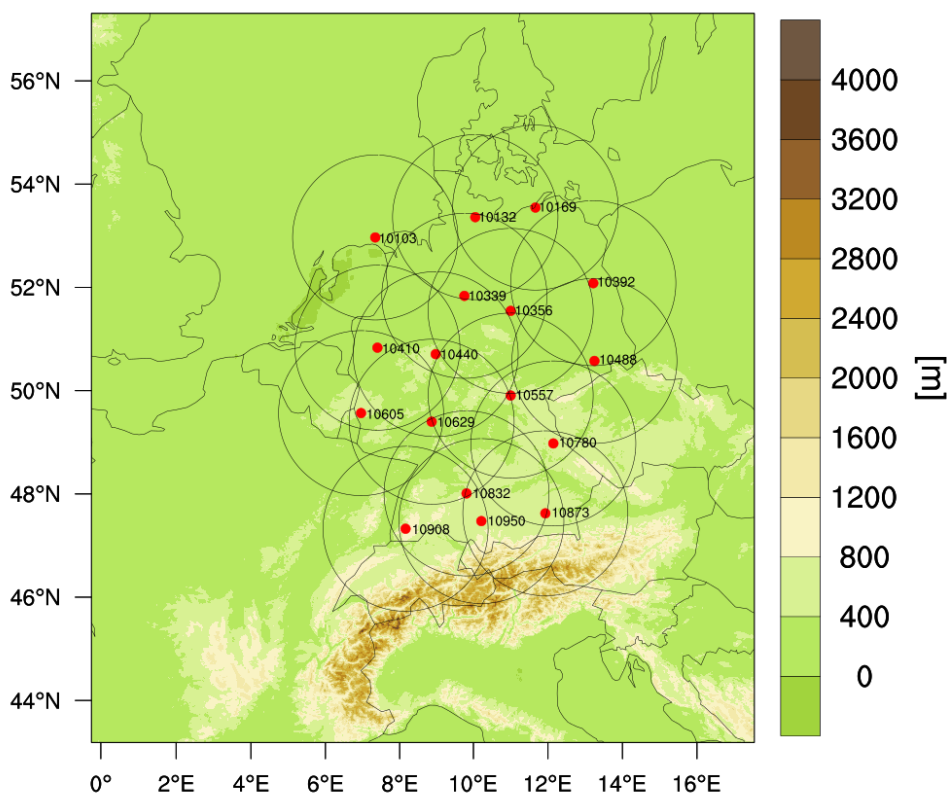
Figure 1. Illustration of the ICON-LAM domain with the orography and of the radar network of the DWD (each station is denoted by a red bullet and the station number, the scanning range is denoted by a circle)

3   The ICON model, radar observations and the observation operator

The ICON (ICOsahedral Nonhydrostatic) global model has been in operation at the DWD since January 2015 (Zängl et al.,
2015), which is non-hydrostatic and is based on an icosahedral (triangular) grid with a horizontal resolution of 13 km and 90
vertical levels. The ICON-LAM (ICON-Limited Area Model) is a regional model with a horizontal resolution of 2.1 km and
65 vertical levels, which became operational since February 2021. Lateral boundary conditions for the ICON-LAM Ensemble
Prediction System (EPS) are provided by the global ICON EPS, with a resolution of 40 (20) km globally and 13 (6.5) km
over Europe for the ensemble (deterministic run). The deep convection is explicitly resolved and the shallow convection is
parametrized with the Tiedtke scheme (Tiedtke, 1989). The turbulent kinetic energy (TKE) scheme for turbulence is developed
by Raschendorfer (2001). The Lin-Farley-Orville-type one-moment bulk microphysical scheme is used, which predicts cloud
droplets q_c, cloud ice q_i, rain q_r, snow q_s and graupel q_g (Lin et al., 1983; Reinhardt and Seifert, 2006).

85

90
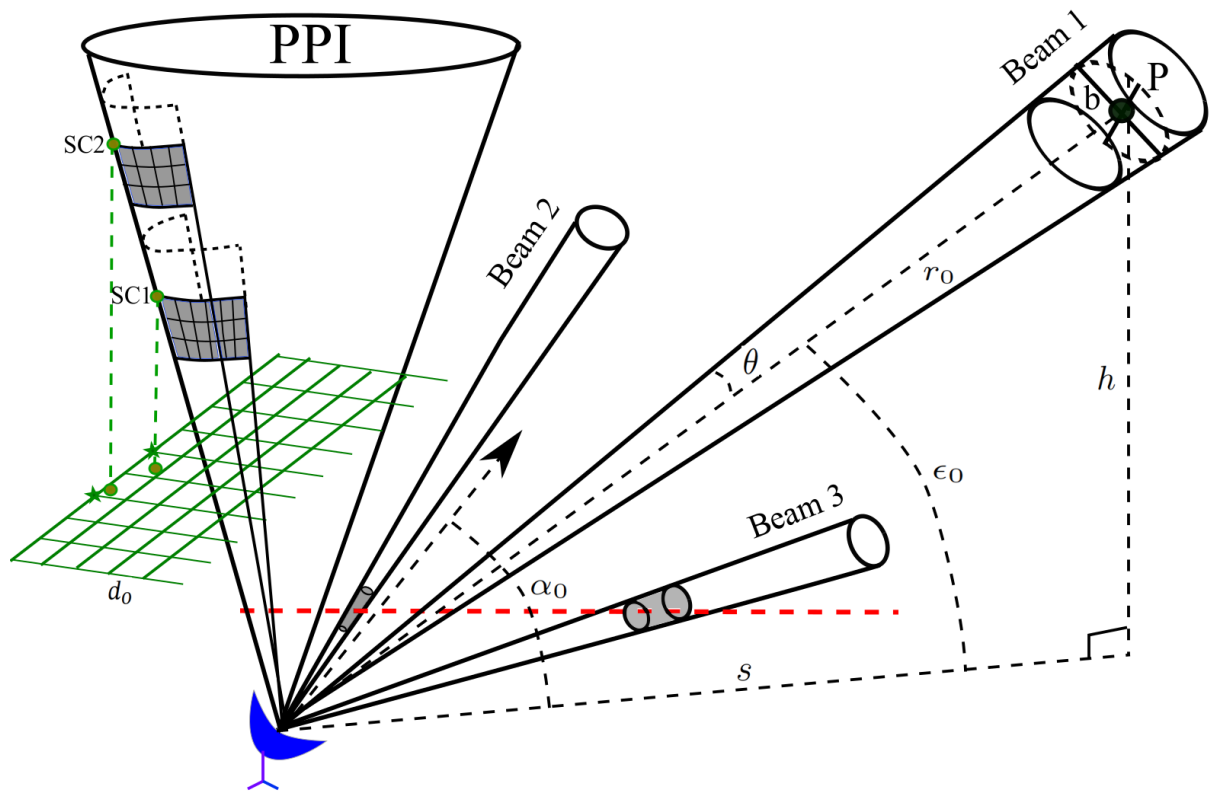
Figure 2. Illustration of the radar coordinate (r, α, ϵ), the beam broadening effect and the superobbing technique: r_0, α_0 and ϵ_0 are the radial range, azimuth and elevation of the beam 1 at the pulse volume whose center is at the point P (denoted by black bullet). h and s are the height and the surface distance of P (note that the curvature of the Earth is omitted in this figure but not in calculations, e.g., in Fig. 3). θ and b are beamwidths in degree and km, respectively. Beam 2 has a higher elevation than Beam 3, the pulse volumes (denoted by grey cylinder) from Beam 2 and Beam 3 are at the same height (dented by red dashed line) but the former one is smaller. The superobbing is done for each PPI scan, individually, for which a Cartesian grid (denoted by green solid line) with a fixed resolution d_o is defined. For each grid point, a point from the PPI scan is searched, whose projection is closest to it. Once it is found, e.g., the point denoted by "SC1", a wedge around it is defined, the grey area is the lower right part of the wedge and the grids denote pulse volumes. SC2 is further in the radial range than SC1 and its superobbing wedge contains fewer pulse volumes.
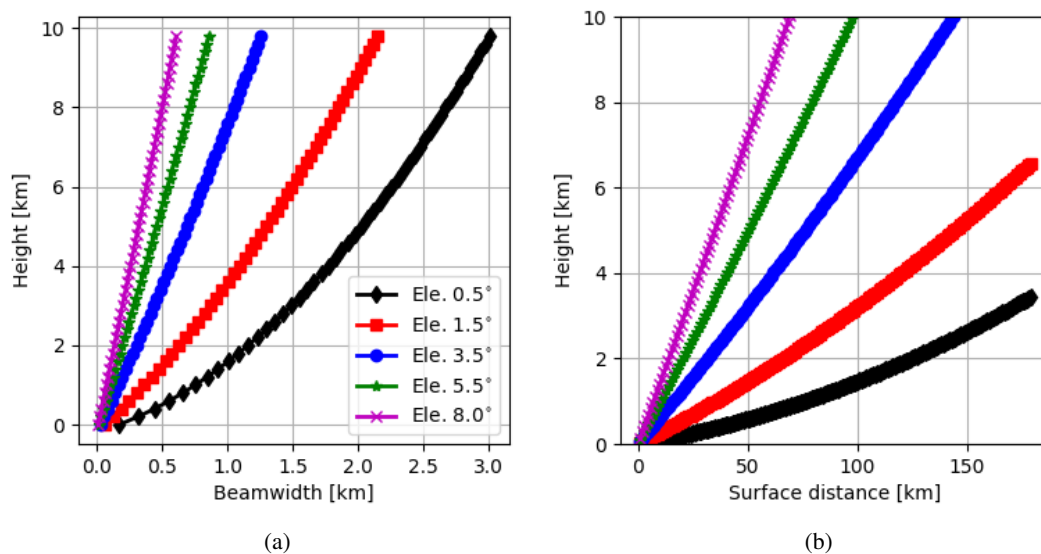
Figure 3. Scratch of variations of beamwidths (in km for azimuth resolution of $1.0°$) with height (left) and surface distances (away from the radar station) with corresponding heights (right) for elevations $0.5°$, $1.5°, 3.5°, 5.5°$ and $8.0°$, based on the 4/3 Earth radius model. The height of the radar station is omitted. The figure for radial ranges with corresponding heights looks very similar to the right panel.

The DWD utilizes a network of 17 C-band Doppler radars covering Germany and part of adjacent countries (see Fig. 1), A complete radar volume scan lasts 5 min and it consists of 180 range bins (resolution of 1.0 km), 360 azimuths (resolution of $1.0°$) and 10 elevations ($0.5°$, $1.5°$, $2.5°$, $3.5°$, $4.5°$, $5.5°$, $8.0°$, $12°$, $17°$, and $25°$). To transform model variables to synthetic radar observations, an Efficient Modular VOlume scanning RADar Operator (EMVORADO, Zeng 2013; Zeng et al. 2014, 2016) has been developed. The EMVORADO is coded in a modular way and is able to simulate effects such as beam bending/broadening/shielding, fall speed and reflectivity weighting for radial wind, attenuation, detectable signal and etc. To simulate reflectivity, two scattering schemes are implemented: the Rayleigh approximation for simple near-spherical hydrometeors whose size is small compared to the wavelength and the Mie method for one- and two-layered spherical hydrometeors of arbitrary size. In the operational setup, the EMVORDAO is run with the Mie method (using look-up tables) and takes beam shielding, fall speed, attenuation and detectable signal into account. Beam bending and broadening effects as well as reflectivity weighting are omitted for the sake of efficiency (computational costs can be found in Zeng et al. 2016). The 4/3 Earth radius model that assumes a standard atmosphere is used to mimic the beam propagation (Zeng et al., 2014).

4 Experimental setup and results

In this section, experiments are performed to create samples for estimation of observation error statistics of radar observations. For each elevation, standard deviations and horizontal correlations at different heights are calculated as Waller et al. (2016c, 2019). Results are shown for elevations $0.5°$, $1.5°$, $3.5°$, $5.5°$ and $8.0°$. The elevations higher than $8.0°$ are not shown due to

small numbers of samples. As in Liu and Rabier (2002); Waller et al. (2016c, 2019), the correlation length scale is determined
by the distance, at which the correlation coefficient is not longer greater than 0.2. Standard deviations are averaged over all
samples and correlations are calculated for each elevation at each radar station for a specific time and then averaged. The
numbers of samples used for estimation of each standard deviation and correlation coefficient are always provided, if the
numbers are around $\sim 10^3$, the estimates are usually statistically insignificant (Waller et al., 2019).

4.1 Observation error statistics estimated by samples of error due unresolved scales and processes

4.1.1 Experimental setup

To create samples for the RE, the ICON-LAM model (equipped with the EMVORADO) is run with a resolution of 1.0 km for
a training period from May 26, 2016, 00:00 UTC to June 25, 2016, 00:00 UTC, which has been investigated in a number of
studies (Zeng et al., 2018, 2019, 2020). During the period, a large area of Southeastern and Central Europe was hit by severe
thunderstorms with heavy rain. The hourly outputs of the model run at 1.0 km are interpolated onto a coarser grid with 2.1
km (operational), and the interpolated states are used as initial conditions for 1-h forecast runs at the resolution of 2.1 km. For
any time during this period, one can build a difference between two model runs. In total, there are 720 samples of differences.
Since the EMVORADO is run together, we have the samples also in radar observation space. Each sample contains differences
in radar volume scans of all radar stations.

It is recognized in Fig. 3a that the resolution of 1 km is still much coarser than the radar beamwidth (although the difference
narrows with increasing height), the RE will be probably underestimated. Nevertheless, the statistics can still provide valuable
insights into features of the RE as shown in the following.

4.1.2 Results

Fig. 4a shows vertical profiles of the estimated standard deviations of the RE for reflectivity that are greater than 5 dBZ (to
be consistent with discussion in Section 4.2) at elevations $0.5°$, $1.5°$, $3.5°$, $5.5°$ and $8.0°$ and Fig. 4b shows the numbers of
samples used ($10^4 \sim 10^6$ near the surface and $\sim 10^4$ at the top). Standard deviations for all elevations are very similar except
at the top, where the higher elevations exhibit slightly smaller errors. It is noticed that the variations of standard deviations are
very comparable to the simulated reflectivities of the (high resolution) model run in Fig. 4c, indicating a systematic error that
is proportional to the true value. By comparing simulated reflectivities in Fig. 4c with the vertical profiles of the mean states of
mixing ratio variables in Fig. 5, it can be deduced that the higher reflectivities below the height of 3 km are mainly attributed
to the rain, the lower reflectivities between 3 and 6 km are due to the increasing amounts of snow which produces lower
reflectivities (cloud ice particles are probably excluded since they can not produce reflectivities greater than 5 dBZ), above 6
km the graupel may dominate, leading to increasing reflectivities. To see the errors decoupled from influences of observations
(this may be interesting for comparison among elevations because different elevations scan different parts of atmosphere, their
measurements may be associated with different errors), the standard deviations are normalized by simulated data from the
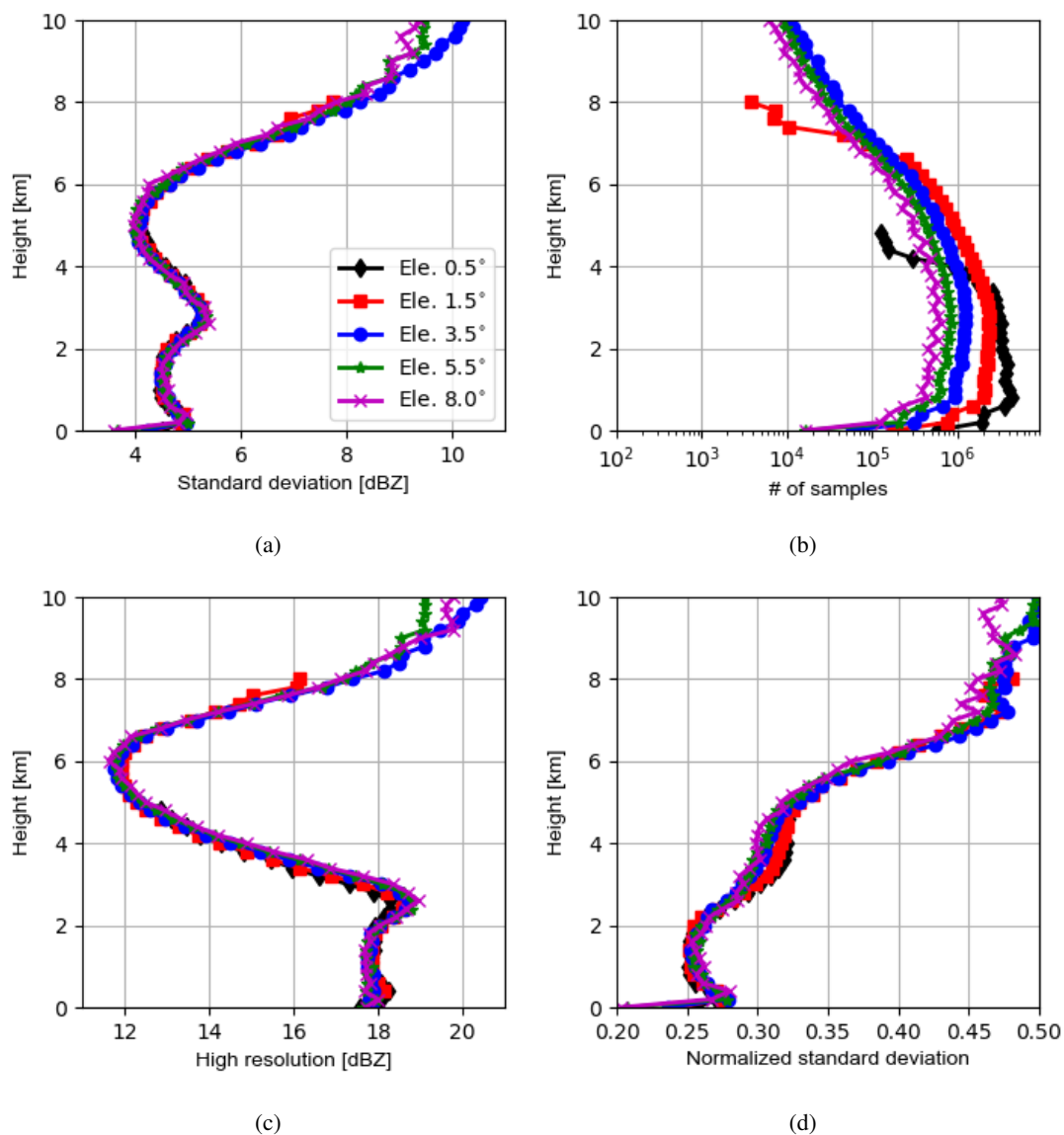
Figure 4. a) Vertical profiles of the estimated standard deviations of the RE for reflectivity data that are greater than 5 dBZ at elevations $0.5°$, $1.5°, 3.5°, 5.5°$ and $8.0°$ b) The numbers of samples used. c) Vertical profiles of simulated reflectivity data greater than 5 dBZ at elevations $0.5°$, $1.5°, 3.5°, 5.5°$ and $8.0°$ in high resolution model run, averaged over all samples; d) Normalized standard deviations of the OE, i.e, standard deviations in a) are divided by high resolution data in c) for each elevation, respectively. For each elevation, the samples are binned every 200 m in the vertical. Here we show results only up to 10 km to be consistent with Section 4.2.
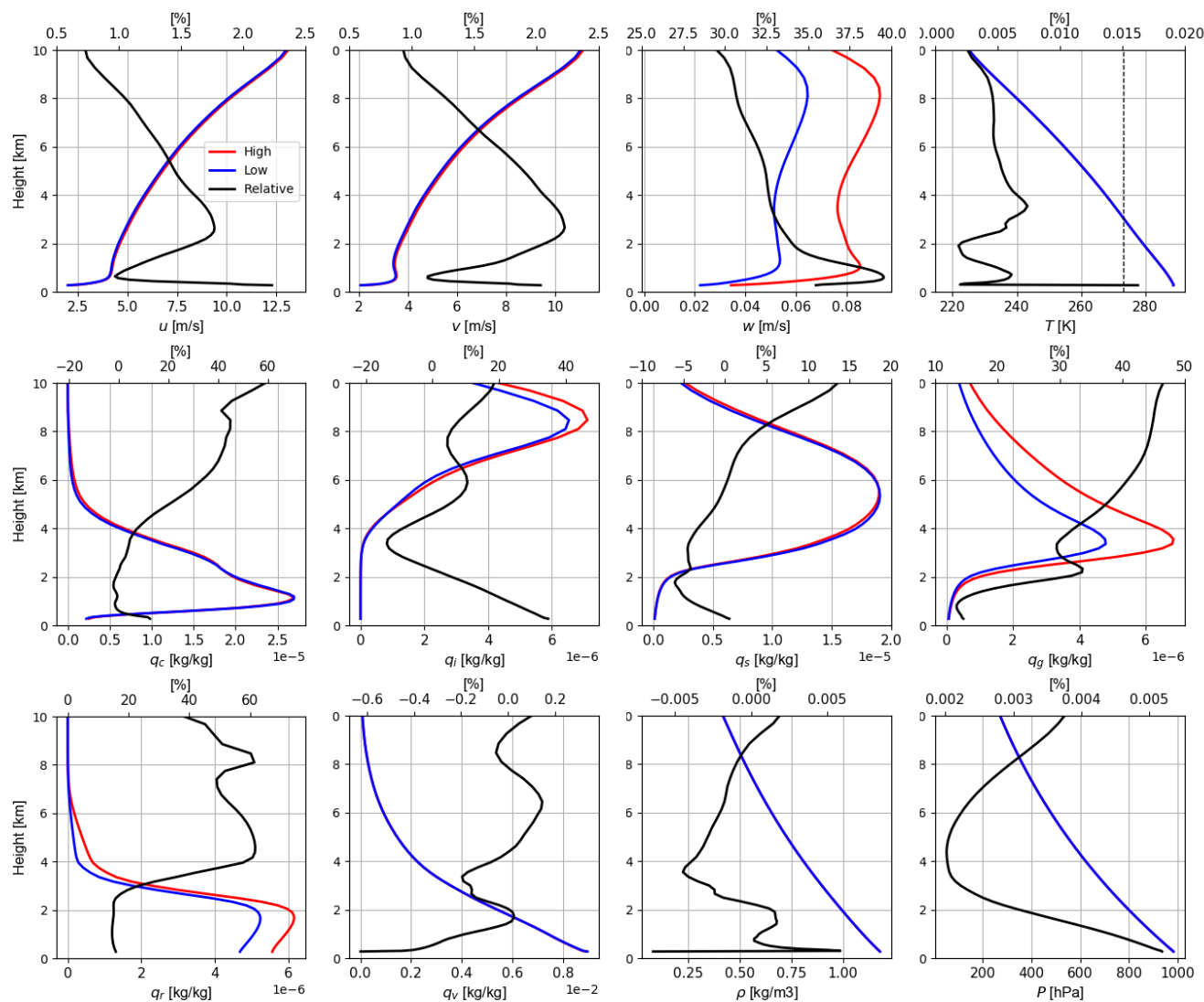
Figure 5. Vertical profiles of model variables such as horizontal wind (u, v), vertical wind w, temperature T, mixing ratios of cloud water q_c, cloud ice q_i, snow q_s, graupel q_g, rain q_r and water vapor q_v as well as air density ρ and pressure P in high (1.0 km) and low resolution (2.1 km) model runs. The absolute values of model variables averaged over the entire period are shown. Black vertical dashed line in Figure for T indicates 273 K. Black solid line is the relative difference [%] (the upper x-axis).
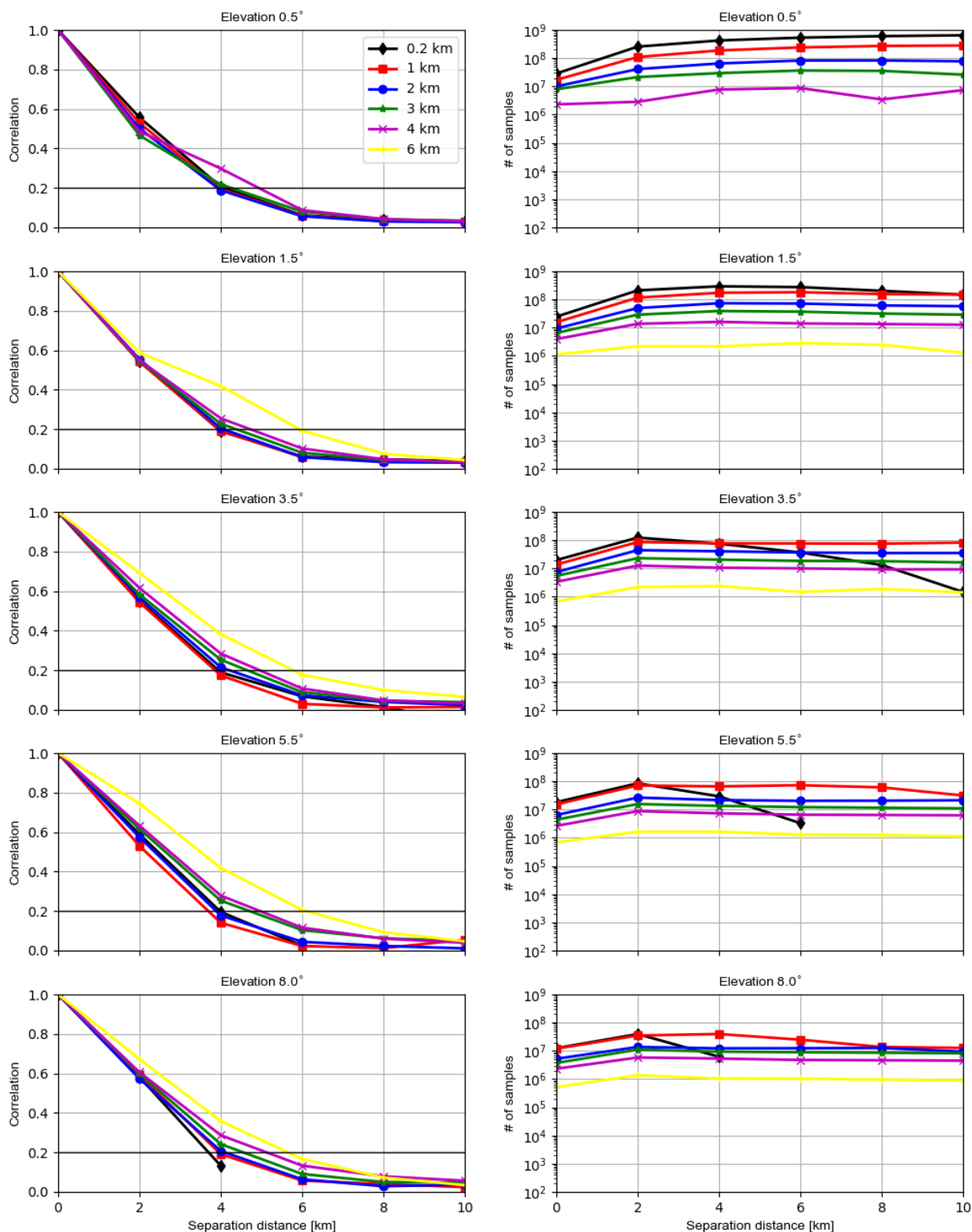
Figure 6. The estimated horizontal correlations of the RE for reflectivity data that are greater than 5 dBZ for elevations 0.5°, 1.5°, 3.5°, 5.5° and 8.0° at heights of 0.2, 1.0, 2.0, 3.0, 4.0 and 6.0 km (left) and the numbers of samples used (right). For each elevation, the samples are binned every 2 km in the separation distance. It is possible for each elevation that samples are not available for some heights.

(a)

(b)

(c)

(d)
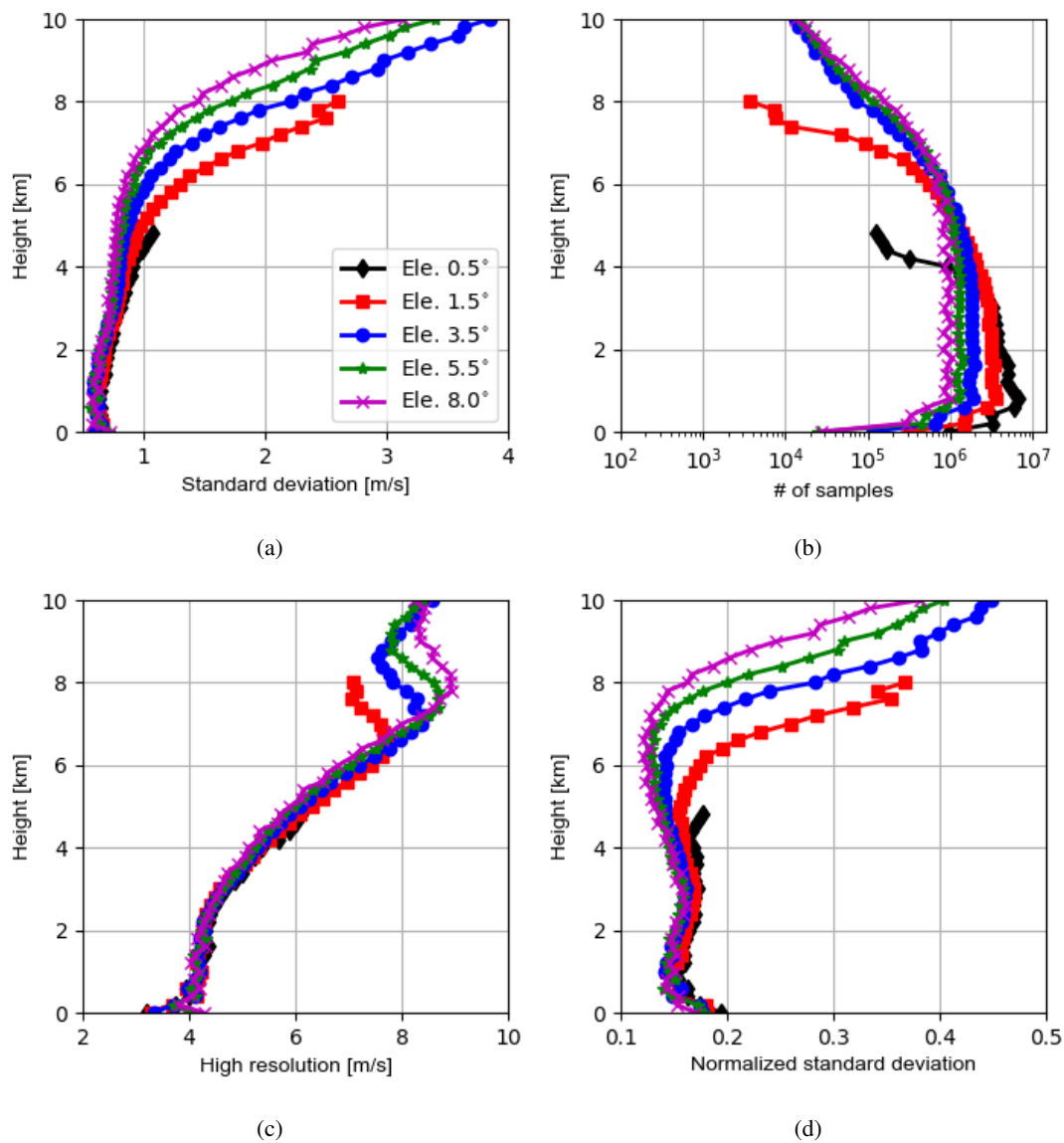
Figure 7. The same as Fig. 4 but for radial wind
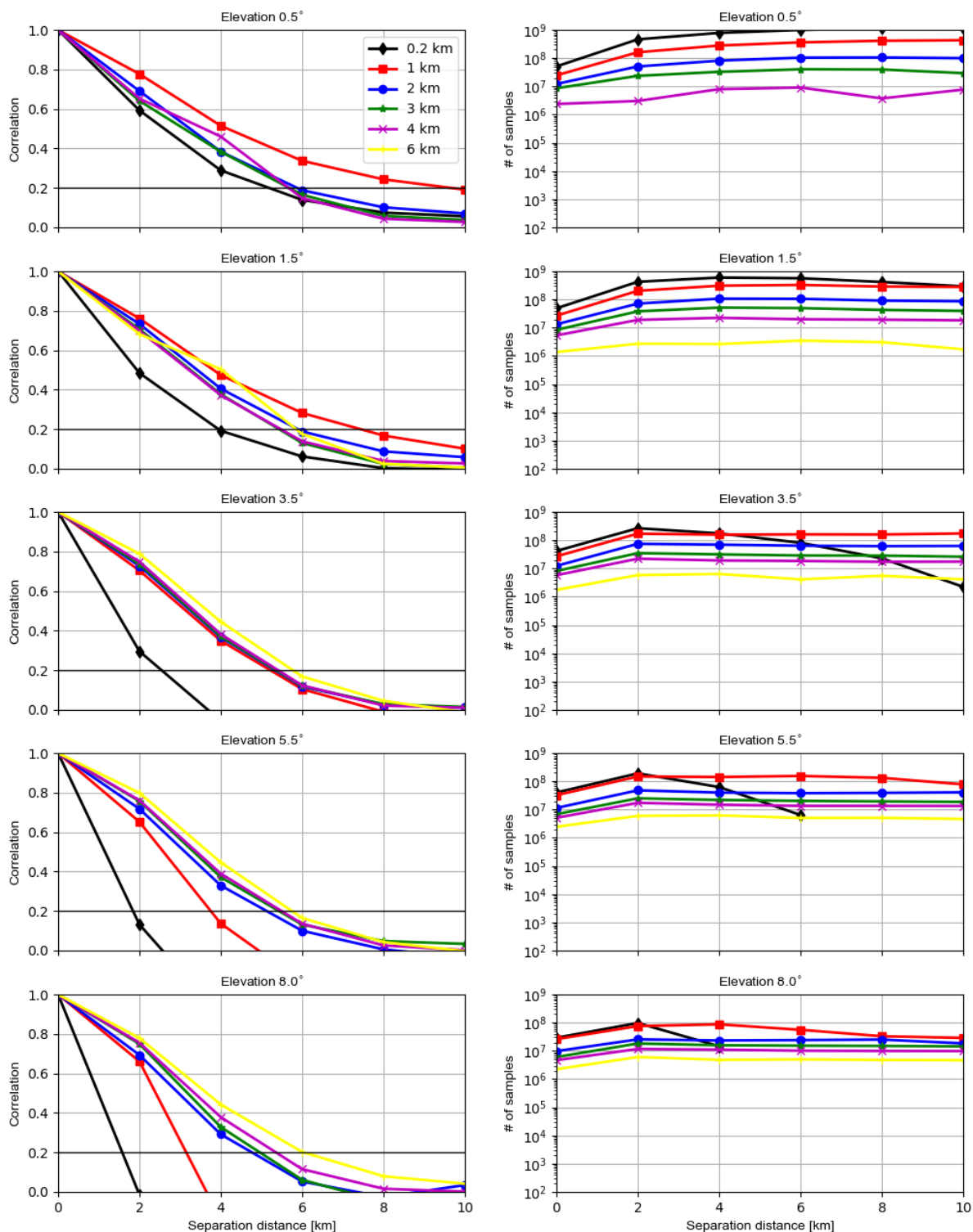
Figure 8. The same as Fig. 6 but for radial wind

high resolution model run that represents the observations. As shown in Fig. 4d, the normalized standard deviations are similar among elevations and they increase consistently with the height.

Fig. 6 shows the horizontal correlations of the RE for reflectivities greater 5 dBZ as well as the numbers of samples used. The numbers of samples are about $10^6 \sim 10^8$ for each separate distance and for each elevation. For the elevation $0.5°$, the correlation length scales at heights of 0.2, 1, 2, 3 and 4 km are given, which are about 4, 4, 4, 4 and 5 km. For $1.5°$, the correlation length scales at the the height of 0.2, 1, 2, 3, 4 and 6 km are given, which are about 4, 4, 4, 4, 5 and 6 km. The correlation length scales for the other higher elevations look similar like for $1.5°$. Overall, it can said that for the same elevation the correlation length scales extend with the increasing height. This can not be owing to the beam broadening effect since it is omitted in both model runs. The reason for this can be attributed to the fact that for higher heights the radar beams have to penetrate longer distances (see Fig. 3b), suffering more from attenuation and likely the other errors, which caused longer correlation length scales. Moreover, for the same height, the correlation length scales exhibit slight sensitivity to different elevations.

The estimated standard deviations of the RE for radial wind and the numbers of samples used ($10^4 \sim 10^7$ at the surface and $\sim 10^4$ at the top) are depicted in Figs. 7a and 7b, respectively. Standard deviations are similar at lower levels for all elevations and they increase with height while standard deviations for lower elevations increase faster. The increase with the height can be simply due to increasing radial wind speed with height (see Fig. 7c). Since the higher elevations are less sensitive to the horizontal wind, smaller standard deviations for the higher elevations suggest that the difference in the horizontal component of the radial wind may dominate the error. The pattern of the normalized standard deviations in Fig. 7d is similar as in Fig. 7a.

The horizontal correlations of the RE for radial wind and the numbers of samples used are given in Fig. 8. The numbers of samples are about $10^6 \sim 10^8$ for each separate distance and for each elevation. For the elevation $0.5°$, the correlation length scales at heights of 0.2, 1, 2, 3 and 4 km are estimated, which are about 6, 10, 6, 6 and 6 km. For $1.5°$, the correlation length scales at the the height of 0.2, 1, 2, 3, 4 and 6 km are estimated, which are about 4, 8, 6, 6, 6 and 6 km. For the other higher elevations, the correlation length scales at the the height of 0.2, 1, 2, 3, 4 and 6 km are given. For the height 0.2 km, the length scales vary from 3 to 2 km for elevations from $3.5°$ to $8.5°$. For 1 km, the length scales vary from 6 to 3 km. For the other heights, the length scales vary from 6 to 5 km. Overall, except 1 km at $0.5°$ and $1.5°$ (the reason for this is unidentified), the length scales lengthens with the increasing heights for the same elevation, which is analogous to reflectivity. However, what is different is that the length scales at the same height become shorter for higher elevations, especially for lower heights. The difference to reflectivity can be due to the fact the radial wind measurement has a directional component and for the same height the lower elevations see more horizontal components of the radial wind than vertical component and the error correlation of the horizontal wind has a much longer length scale (see Figure 5 of Zeng et al. 2019). Furthermore, the correlation length scales for reflectivity are generally a bit shorter for lower elevations, this may be because the error correlation length scales of mixing ratio variables are shorter than those of the horizontal wind, but for higher elevations, the role of vertical component of the radial wind amplifies and shortens the correlation length scales.
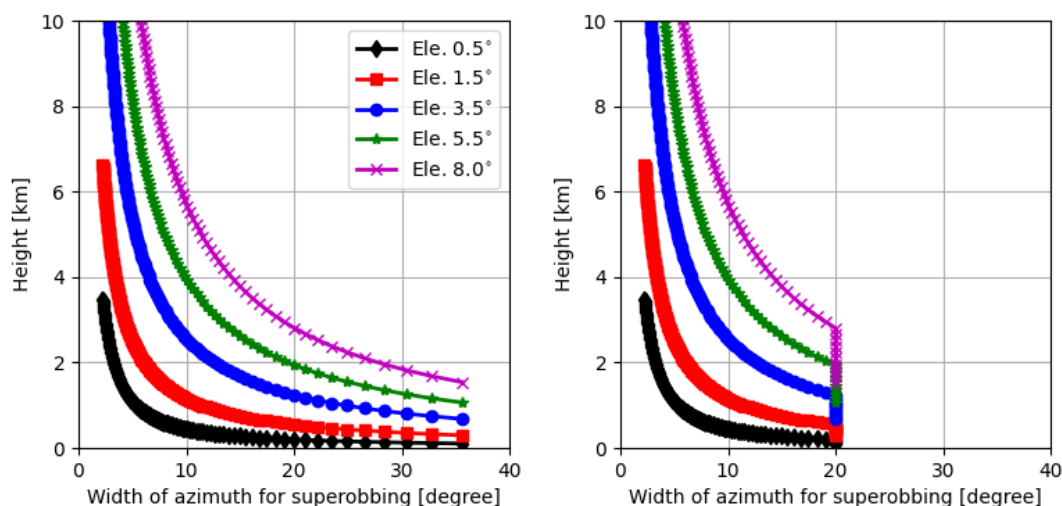
Figure 9. Variations of the width of azimuth with height for superobbing reflectivity (left) and radial wind (right) at elevations $0.5°$, $1.5°, 3.5°, 5.5°$ and $8.0°$. A maximum of $20°$ is set for superobbing radial wind.

4.2 Observation error statistics estimated by the Desroziers method

4.2.1 Experimental setup

175 To apply the Desroziers method, data assimilation experiments are run with hourly update from 03 June to 17 June 2019. During this summer time, severe thunderstorms affected large parts of Germany. We use the operational ICON-LAM KENDA system. The ensemble size is 40 and a deterministic run is updated by the Kalman gain for the ensemble mean. The main data assimilation scheme is the LETKF, via which conventional observations including radiosondes (TEMP), wind profilers (PROF), aircraft reports (AIREP) and synoptic surface observations (SYNOP) as well as MODES data (Lange and Janjić,

180 2016) are assimilated. More details about the usage of those observations can be found in Schraff et al. (2016).

In addition, radar observations are also directly assimilated by the LETKF via using the radar observation operator EMVO-RADO. Prior to assimilation, signal processor filters (Werner, 2014) are applied to radar observations for quality control. Due to high density, radar observations are thinned in time and space. Temporally, only the latest 5 min radar observations prior to the analysis time are assimilated (Zeng et al., 2018, 2019, 2020, 2021a, b; Gastaldo et al., 2021). Spatially, the superob-

185 bing technique is applied to each PPI scan (see Fig. 2), with the goal of obtaining homogeneous distributions of observations in horizontal. The following explains how it works: first, a horizontal Cartesian grid with a desired resolution d_o is defined. Second, for each Cartesian grid point, the algorithm searches for the closest radar bin. If the bin is not too close to the radar station (within radial range of 10 km), it will be regarded as the center of superobbing. Third, a wegde-shaped area around the center bin is defined by the radial range interval and the azimuth width. The radial range interval is given by $\pm\dfrac{d_o\sqrt{2}}{2}$

190 and the azimuth width at the radial range r_0 is given by $\pm\arctan\left[(d_o\sqrt{2}/2)/r_0\right]$. The superobservation is then created by
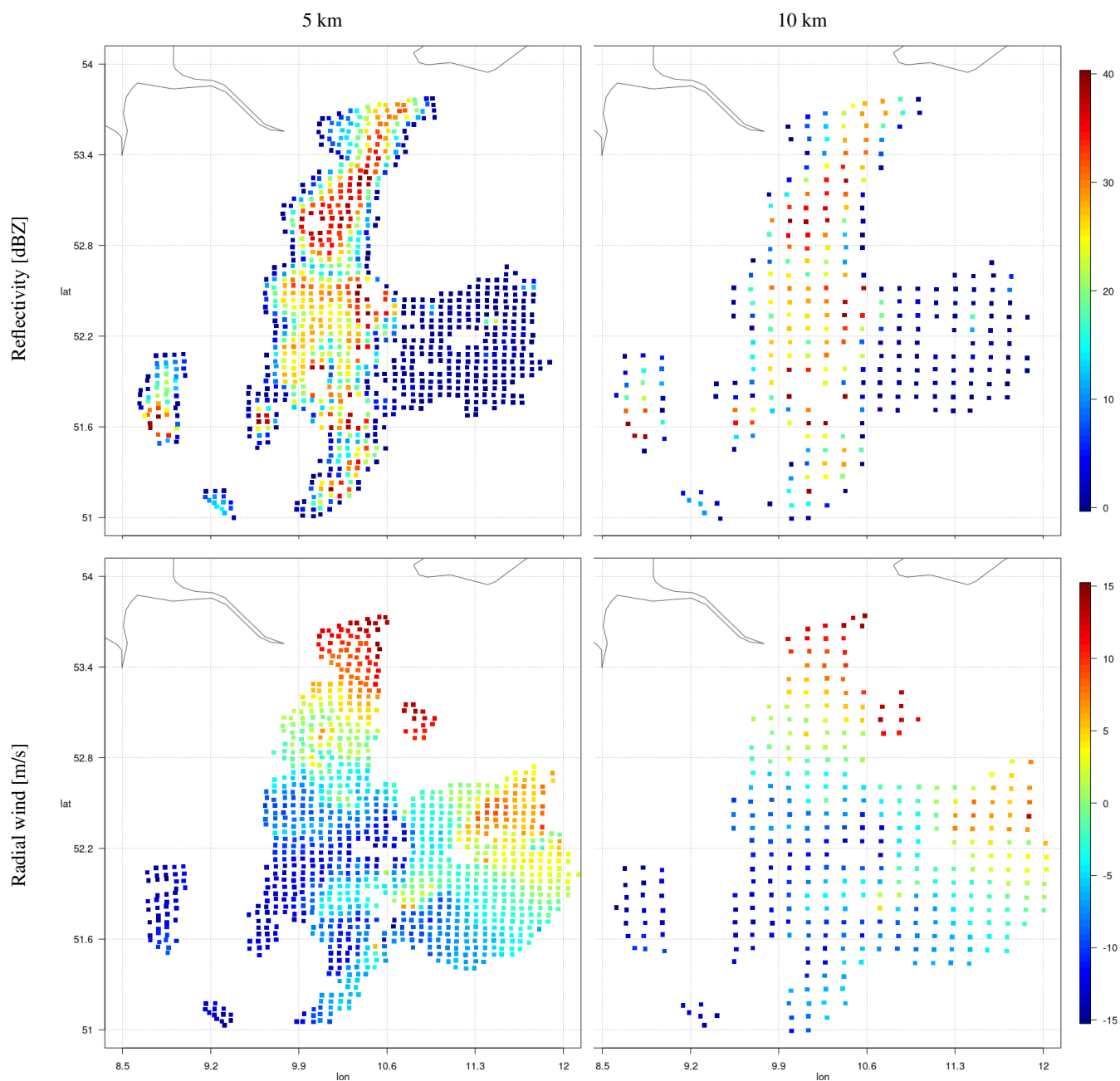
Figure 10. Illustration of superobbing for reflectivity (upper) and radial wind (lower) with resolution $d_o = 5$ km (left) and $d_o = 10$ km (right) at elevation $0.5°$ for the radar station 10356 at 13:00 UTC June 3, 2019

averaging raw observations within the wedge area. Note that: 1) before superobbing, the modelled radial wind is dealiased (the folding speed is 32 m/s), and all reflectivities lower than 0 dBZ are set to be 0 dBZ in both simulations and observations and

treated as no reflectivity data (Aksoy et al., 2009). 2) If there are fewer than three raw observations within the wedge area, the superobservation will be discarded. Additionally for the radial wind, the azimuth width is limited to $20°$, and if the standard
195 deviation of raw observations exceeds 10 m/s, the superobservation will be discarded. Second and third steps are repeated for all PPI scans. As noted by Waller et al. (2019), this superobbing technique may create error correlations since the same raw observations may be accounted for in neighboring superobservations. This occurs more often for the lower heights (or near ranges) since the the azimuth width decrease with increasing height (see Figs. 2 and 3a). In this study, we set $d_o = 5$ km. An example of superobservations at elevation $0.5°$ is given in Fig. 10. In addition to the LETKF, the latent heat nudging (LHN) is
200 performed for each ensemble member and the deterministic run to assimilate radar-derived precipitation rates (Stephan et al., 2008).

For specification of the $\mathbf{R}$, a diagonal matrix is used. For the radar reflectivity, $\mathbf{R} = 10 \cdot 10 \cdot \mathbf{I}$ [dBZ^2], where $\mathbf{I}$ is the identity matrix. For the radial wind, $\mathbf{R} = 2.5 \cdot 2.5 \cdot \gamma \cdot \mathbf{I}$ [m^2/s^2]. Since the radial wind measurements are of lower quality for lower reflectivities, a scaling factor γ is introduced, which varies between 1.0 and 10.0 depending on reflectivities and is determined
205 by the EMVORADO. For reflectivities smaller than 0 dBZ, $\gamma = 10.0$, for reflectivities greater than 10 dBZ, $\gamma = 1.0$, and for reflectivities inbetween, γ decreases linearly. Before (super)observations are assimilated, a first guess check is carried out, which compares the first guess departure of the deterministic run with the sum of the ensemble spread and $\mathbf{R}$ and rejects the (super)observations if the difference is too big. For localization, an adaptive localization is applied in horizontal for conventional data, whose radius is bounded between 50 and 100 km, and the radius of vertical localization varies with altitude from
210 0.0075 to 0.5 in logarithm of pressure. For radar observations, the localization radius in horizontal is constant and set to be 16 km. The observations are weighted by the 5-th order Gaspari-Cohn function (Gaspari and Cohn, 1999). For inflation, adaptive multiplicative inflation, relaxation to prior perturbations (RTPP, Zhang et al. 2004) and large-scale additive noise (Zeng et al., 2018) are jointly applied. The prognostic variables are updated at the analysis step except the precipitating variables (i.e., q_s, q_g and q_r). Also note that boundary layers including 67 km lateral boundaries at each side and heights above 300 hpa
215 (approximately 10 km) are not updated.

4.2.2 Results

As Waller et al. (2019), we use the first guess and analysis departures of the deterministic run to calculate the statistics of the OE. Fig. 11 shows vertical profiles of the estimated standard deviations of the OE for reflectivity at elevations $0.5°$, $1.5°$,$3.5°$,$5.5°$ and $8.0°$ as well as the numbers of samples used ($10^3 \sim 10^6$, the higher the elevations is, the fewer samples are available). It
220 is noticed that the standard deviations vary between 4 and 7 dBZ, which is much smaller than 10 dBZ that is used to assign $\mathbf{R}$. This is due to the treatment setting all negative values of reflectivity equal to 0 dBZ in both observations and simulations for assimilating no reflectivity data, which reduces first guess and analysis departures and thus results in smaller estimated errors (see also Zeng et al. 2021a). To show the "real" errors, only reflectivity greater than 5 dBZ are evaluated in Fig. 12. Compared to statistics shown in Section 4.1, the OE obtained here are subject to new error sources such as the IE and FE, as well as a
225 larger RE since the real radar observations have a even finer resolution than 1 km that is used in Section 4.1. Nevertheless, standard deviations in Fig. 12a exhibit considerable similarity as in Fig. 4a, indicating that the RE may be an dominant error
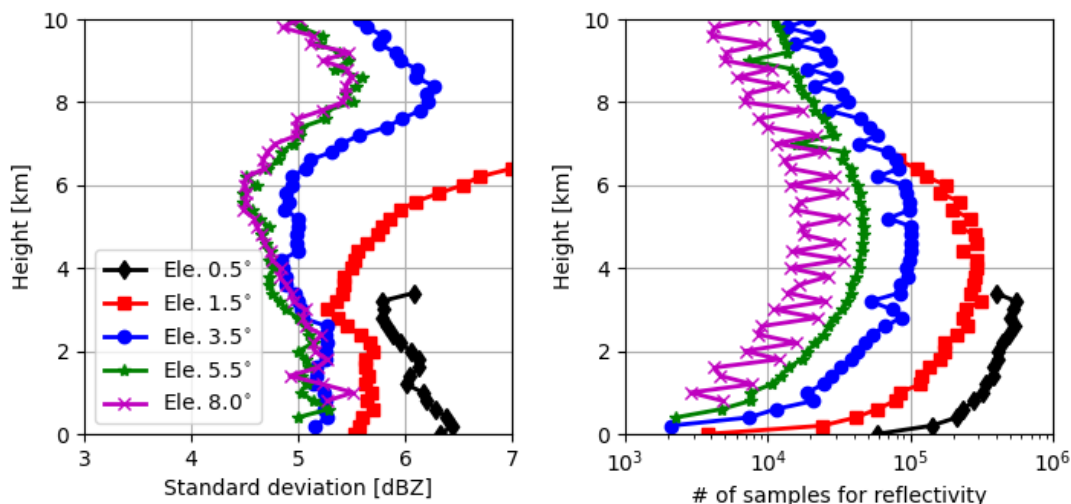
Figure 11. Vertical profiles of the estimated standard deviations of the OE for reflectivity data (including no reflectivity data) at elevations $0.5°$, $1.5°$, $3.5°$, $5.5°$ and $8.0°$ (left) and the numbers of samples used (right). For each elevation, the samples are binned every 200 m in the vertical. Since model states are not updated above 10 km, standard deviations continuously increase (see Waller et al. 2019). Here we show results only up to 10 km.

source. Comparing Fig. 12c with Fig. 4c, it is seen that simulated reflectivities are much higher than observations between 6 and 8 km, this may be because the model produces too much graupel over there. The decrease of the standard deviations above 8 km can be attributed to the reduction of excessive graupel in model simulation. The difference to Fig. 4a also lies in that the

230 standard deviations of different elevations are quite different in Fig. 12a, and at the same height the lower elevations are, the larger are the standard deviations.This can be attributed to a larger IE that occurs while the lower elevations scanning longer distances as well as to a larger FE that the pulse volume of lower elevations are larger (see Fig. 2) and the beam broadening effect is omitted in the EMVORADO. Moreover, the larger error of elevation $0.5°$ at the surface is probably due to the ground clutter. Finally, Fig. 12d shows that the increase of the normalized standard deviations continues until 8 km and halts. All

235 elevations are similar except that the elevation $0.5°$ is associated considerably larger errors below 1 km.

Fig. 13 shows the horizontal correlations of the OE for reflectivities greater 5 dBZ as well as the numbers of samples used (correlations for reflectivities including no reflectivity data are not shown because they exhibit very similar patterns as in Fig. 13). For the elevation $0.5°$, the correlation length scales at the the height of 0.2, 1.0, 2.0 and 3.0 km are given, which are about 20, 20, 25 and 40 km, based on $10^5 \sim 10^6$ samples. For $1.5°$, the correlation length scales at the the height of 0.2,

240 1.0, 2.0, 3.0, 4.0 and 6.0 km are given, which are about 20, 20, 25, 30, 35 and 50 km, based on $10^4 \sim 10^5$ samples. For $3.5°$, the correlation length scales at the the height of 1.0, 2.0, 3.0, 4.0 and 6.0 km are given, which are about 20, 25, 35, 35 and 50 km, based on $10^4 \sim 10^5$ samples. For $5.5°$ and $8.0°$, the correlations at the the height of 2.0, 3.0, 4.0 and 6.0 km are a bit fluctuating due to small numbers of samples used ($10^3 \sim 10^4$) but the patterns are comparable to $3.5°$. Overall, it is analogous
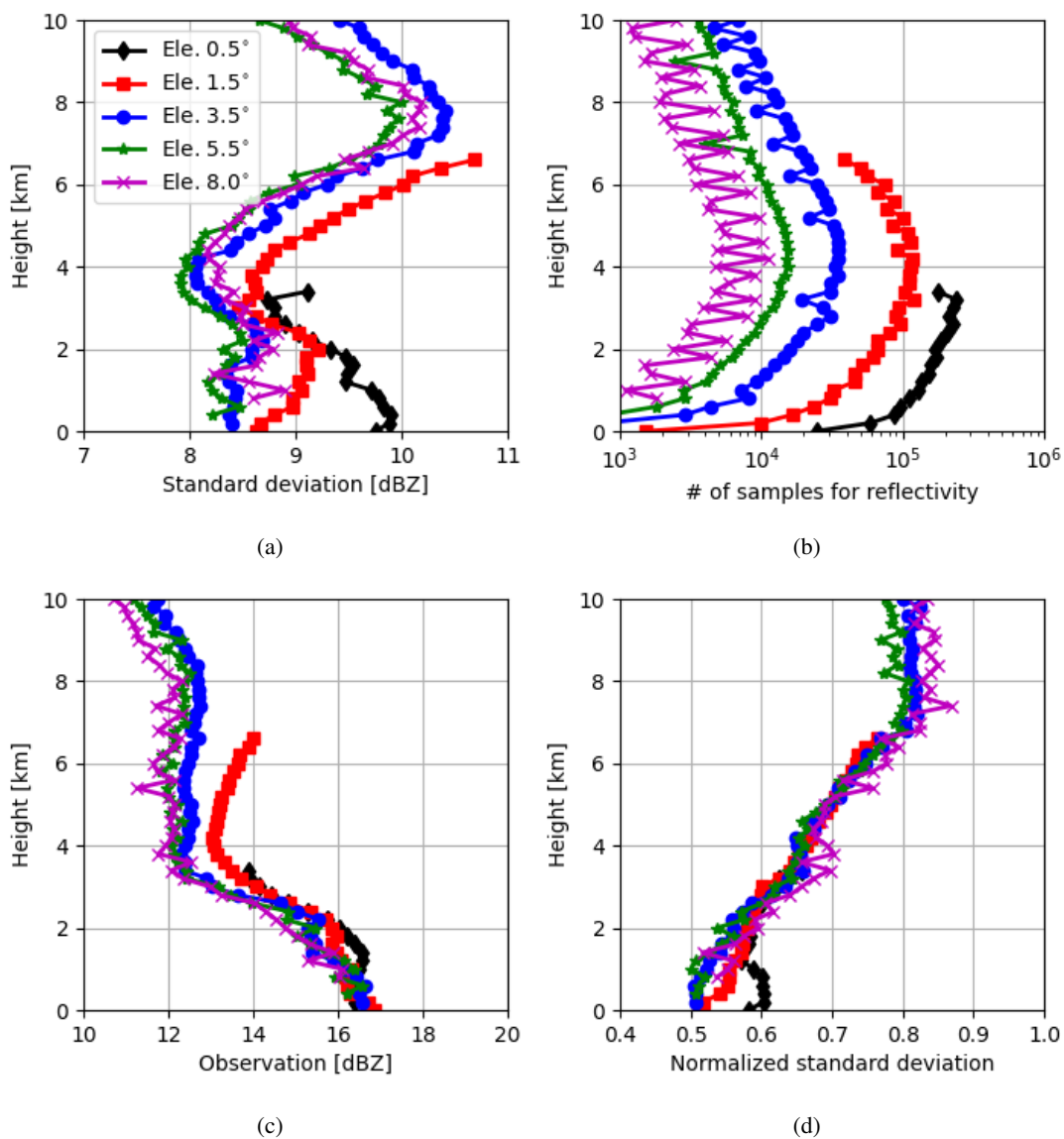
Figure 12. a) and b) are the same as Fig. 11 but for reflectivity data that are greater than 5 dBZ; c) Vertical profiles of observed reflectivity data greater than 5 dBZ at elevations 0.5°, 1.5°,3.5°,5.5° and 8.0°, averaged over all samples; d) Normalized standard deviations of the OE, i.e, standard deviations in a) are divided by observed data in c) for each elevation, respectively.
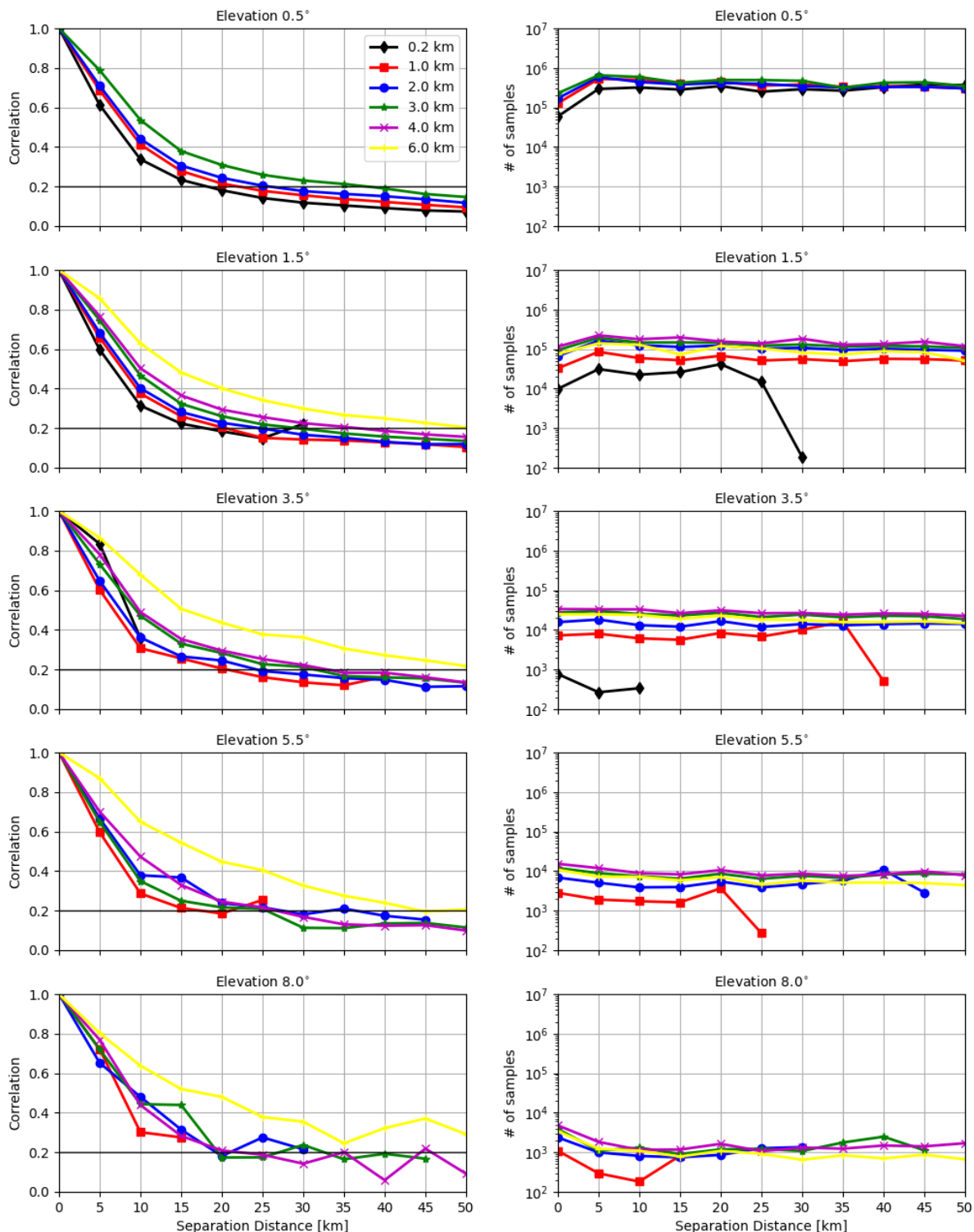
Figure 13. The estimated horizontal correlations for the observation error of reflectivity data that are greater than 5 dBZ for elevations 0.5°, 1.5°,3.5°,5.5° and 8.0° at heights of 0.2, 1.0, 2.0, 3.0, 4.0 and 6.0 km (left) and the numbers of samples used (right). For each elevation, the samples are binned every 5 km in the separation distance.
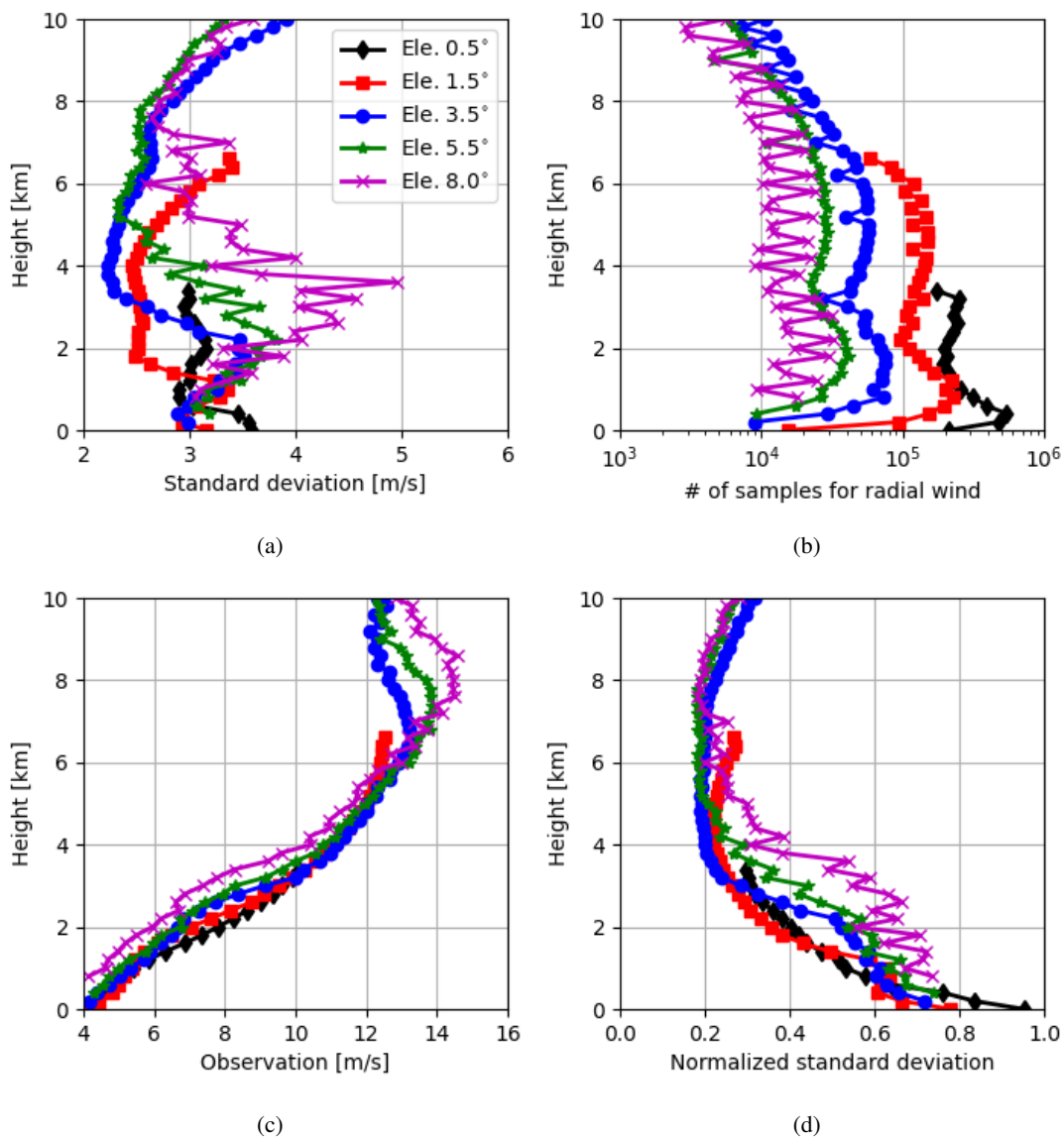
Figure 14. The same as Fig. 12 but for radial wind data
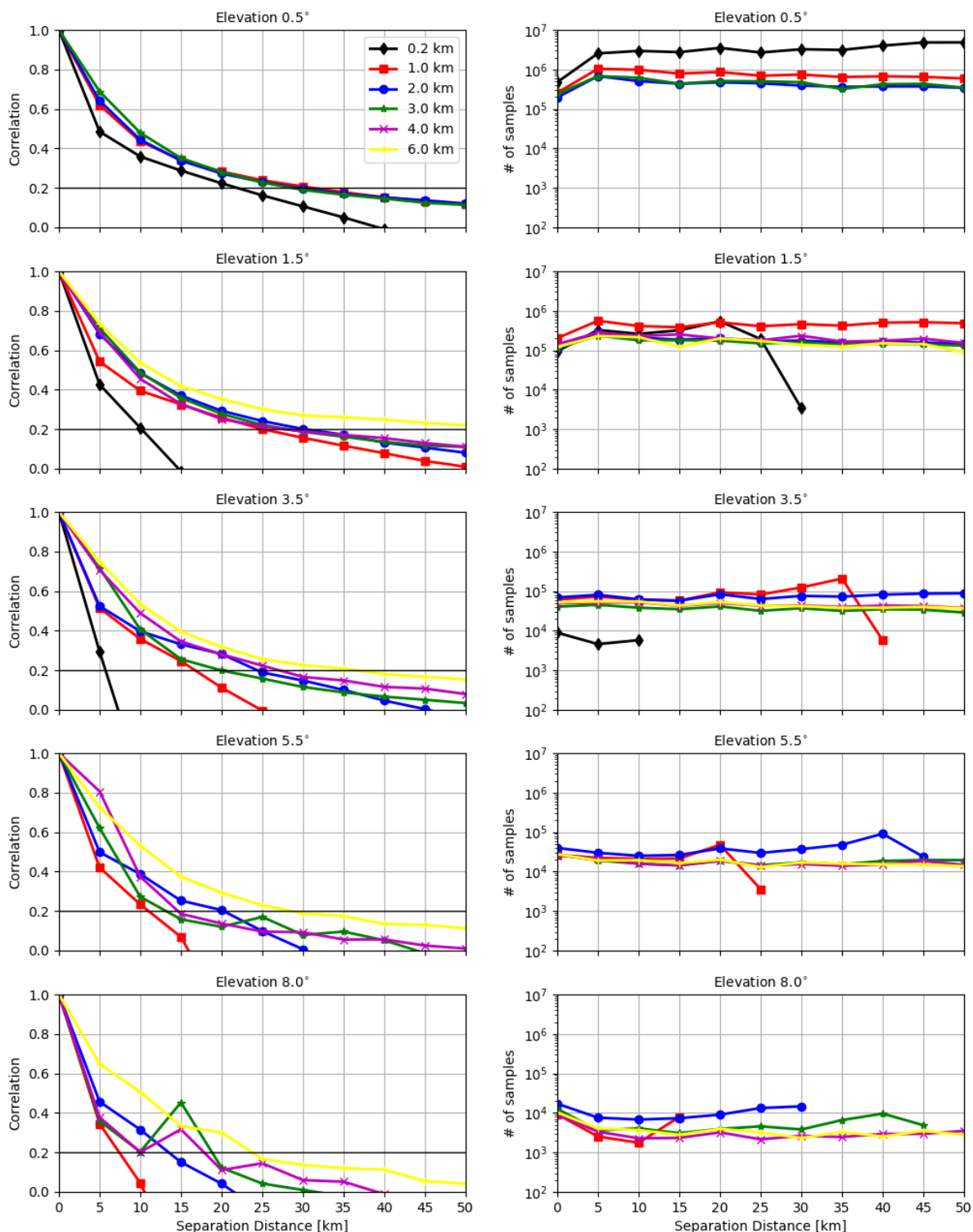
Figure 15. The same as Fig. 13 but for radial wind data

to Fig. 6 that for the same height the correlation length scales exhibit no sensitivity to different elevations and that for the same

245   elevation the correlation length scales increase with the height, the latter one is due to the fact that for higher heights the radar beams have to reach out longer distances. Furthermore, as argued in Waller et al. (2016c), the increasing pulse volume at longer distances could be another factor since the the beam broadening effect is omitted in the EMVORADO. It is also noticed that the length scales are much longer than those in Fig. 6. In addition to these two reasons just mentioned, the superobbing can be also responsible for longer length scales. In an experiment with the superobbing resolution of 10 km (here 5 km), the lengths

250   scale are generally increased by 5 km (not shown). The error caused by the superobbing is usually considered as a type of FE (Janjic et al., 2018).

Fig. 14a shows vertical profiles of the estimated standard deviations of the OE for radial wind at elevations $0.5°$, $1.5°$, $3.5°$, $5.5°$ and $8.0°$ and Fig. 14b shows the numbers of samples used ($10^3 \sim 10^6$, the higher the elevations is, the fewer samples are available). The variation patterns of standard deviations are similar to Waller et al. (2019) although the values here are greater due

255   to the application of scaling factor for $\mathbf{R}$. It is noticed in Fig. 14a that between 1 and 6 km the higher elevations are generally associated with larger errors, which is quite different to Fig. 7a. Since higher elevations see more in the vertical, this suggests that the vertical component of the radial wind is not well reproduced. On one hand, it can be related to the misrepresentation of w in the model (see large differences caused by changing the model resolution from 2.1 to 1 km in Fig. 5 and considering that for heights till 6 km the radar beamwidth is much shorter than 1 km for higher elevations (see Fig. 3a)). Small-scale strong

260   updrafts often occur within these heights, which radar observations can much better resolve than the model, leading to a larger RE. On the other hand, it can be also related to the misrepresentation of the terminal fall speed of hydrometeors, which can be due to the parametrization in the microphysical scheme and which can also be due to neglecting reflectivity weighting of the radial wind in the EMVORADO. It is shown in Zeng et al. (2016) for an idealized supercell case that the hydrometeor terminal fall speed with the reflectivity weighting can be maximal 8 m/s faster than without. This causes a larger FE. With increasing

265   height, the misrepresentation of the vertical component becomes less (due to the increasing pulse volume) or less pronounced (due to the increasing horizontal wind speed, and the standard deviations become smaller. Above 6 km, anvil regions are approached where divergent convective outflows occur and winds move in different directions and slight spacial shifts of cells in simulations can lead to large errors, therefore, the standard deviations increase. In Fig. 14d, it can be better seen that the errors decrease with height up to 6 km due to better representation of the vertical component and then increase when it get closer to

270   anvil regions.

Fig. 15 shows the horizontal correlations of the OE for the radial wind as well as the numbers of samples used. For the elevation $0.5°$, the correlation length scales at the the height of 0.2, 1.0, 2.0 and 3.0 km are given, which are about 20, 30, 30 and 30 km, based on $10^5 \sim 10^7$ samples. For $1.5°$, the correlation length scales at the the height of 0.2, 1.0, 2.0, 3.0, 4.0 and 6.0 km are given, which are about 10, 20, 25, 25, 25 and longer than 50 km, based on $10^5 \sim 10^6$ samples. For $3.5°$, the correlations

275   length scales at the the height of 1.0, 2.0, 3.0, 4.0 and 6.0 km are given, which are about 20, 25, 20, 30 and 35 km. For $5.5°$ and $8.0°$, the correlations at the the height of 1.0, 2.0, 3.0, 4.0 and 6.0 km are a bit noisy due to small numbers of samples used ($10^3 \sim 10^5$), but overall it still can be seen that for the same elevation the correlation length scales increase with the height, this is the same as the reflectivity. Generally, it is also seen that the lower elevations exhibit longer correlation lengths for the

same height, which is different to reflectivity. This can be due to the fact the radial wind is a directional measurement and the

280 lower elevations see more contributions from the horizontal wind than from the vertical velocity and the error of the former one has generally a longer correlation length scale.

5 Summary and discussion

An adequate specification of the observation error (OE) covariance can be beneficial for convective-scale radar data assimilation since the radar measurements are dense and their errors are strongly correlated. The Desroziers method has been used in

285 previous studies to calculate the variances and correlations of the OE for radial wind data (e.g., Waller et al. 2016c, 2019). However, the estimated statistics are not fully understood since they are composed of contributions from different sources such as instrument error (IE), the observation operator error and pre-processing or quality control error as forward model error (FE) and the error due to unresolved scales and processes (RE) and it is difficult to distinguish individual portion (Janjic et al., 2018). To better understand possible contributions of the RE, another approach is proposed, which assumes a high resolution model

290 run as truth and a low resolution model run as a truncation, and a set of samples for truncation error are created and used to approximate the statistics of the RE.

In this work, we have run the ICON-LAM model (equipped with the radar observation operator EMVORADO) with resolutions of 1.0 and 2.1 km in a coupled manner for a summer convection period and a sufficient amount of samples for truncation error in radar observation space have been obtained. The statistics of samples are evaluated for each elevation. It is found for

295 the reflectivity that the standard deviations of the RE are similar for all elevations and is a systematic error proportional to the true value. For the same elevation, the horizontal correlation length scales increase with height, which can be attributed to the fact that for higher heights the radar beams have to travel through longer distances. For the same height, the correlation length scales are not sensitive to different elevations. Similar can be seen for the radial wind except that at the same height the length scales become shorter for higher elevations, especially for lower heights, which can be due to the fact the radial wind

300 measurement has a directional component and for the same height the lower elevations see more horizontal components of the radial wind than vertical component and the error correlation of the horizontal wind has a much longer length scale. Furthermore, the correlation length scales for reflectivity are generally a bit shorter for lower elevations, this may be because the error correlation length scales of mixing ratio variables are shorter than those of the horizontal wind, but for higher elevations, the vertical component of the radial wind shortens the correlation length scales.

305 Besides, we have performed data assimilation experiments with the ICON-LAM KENDA system for another summer convection period, using the (almost) operational setup. We have used the Desroziers method to estimate the statistics of the OE. Results show that due to treatment of no reflectivity the standard deviations of reflectivity data are much smaller than the OE is used in the data assimilation system. The standard deviations of reflectivities greater than 5 dBZ exhibit a comparable pattern to that of the RE, indicating the RE is likely a dominant error source. The difference to the RE also exists. The standard deviations

310 of different elevations are quite different, i.e., at the same height, the lower elevations are, the larger are the standard deviations. This can be caused by a larger IE that occurs while the lower elevations scanning longer distances and a larger FE that the pulse

volume of lower elevations are larger but the beam broadening effect is omitted in the EMVORADO. Furthermore, it is found that the model produces too much ice above 6 km, which needs to be improved in the future. For radial wind data, the standard deviations of the OE are much larger than those of the RE, this is mainly due to the the application of scaling factor for the OE

315   used in the data assimilation system. The scaling factor inflates the OE where the reflectivity values are too small ($\leq$ 10 dBZ). Besides, the standard deviations are especially large between heights of 1 and 6 km for the higher elevations. This can be caused by the misrepresentation of the vertical wind in the model since the the vertical wind is very sensitive to the model resolution, it can also be caused by the misrepresentation of the terminal fall speed of hydrometeors due to inaccuracy in parametrization of the microphysical scheme and to neglection of reflectivity weighting of the radial wind in the EMVORADO. With respect to

320   the correlation length scales of the OE, for both reflectivity and radial wind data, the length scales behavior similarly as those of the RE but the length scales are much longer. Among the possible error sources mentioned above, the application of the superobbing is another reason. Shorter superobbing resolution reduces the length scales. However, considerable correlations still exist, which indicates the necessity of including correlations in the OE covariance matrix for radar data.

Overall, it is successful to use the statistics of truncation error in observation space to better understand the statistics of

325   the OE estimated by the Desroziers method. The RE contributes greatly to the variances and defines some features in the correlation length scales. It is noted that using the Desroziers method for reflectivity and no reflectivity data together always results in too small variances. If one considers using them for data assimilation, one should inflate them or separate reflectivity and no reflectivity data in advance. Besides, one should keep in mind that the Desroziers method tends to produce too small variances as shown in a number of studies (Weston et al., 2014; Bormann et al., 2016). In contrast, the variances of the radial

330   wind is considerably large due to scaling, it may be unnecessary to inflate them for the further use. Comparing the statistics of the RE and OE, we see the potential in improving the microphysical scheme and the necessity of using a more comprehensive configuration of the EMVORADO (or even improvement). We may also consider refining the superobbing strategy to avoid creating correlations. The statistics presented here can be also used as a guideline for selecting which observations to assimilate and for assignment of the OE covariance matrix that can be diagonal or full and correlated.

335   *Code and data availability.*

All the data upon which this research is based are available through personal communication with the authors. Access to the source code of the ICON model is restricted to ICON licenses. A license can be obtained for research if following the procedure described at https://code.mpimet.mpg.de/projects/icon-license.

Author contributions.

340   Y. Zeng provided the idea, conducted the data assimilation experiments and wrote the first draft of the paper. Y. Feng conducted the experiments for creation of samples of truncation error and evaluated them. T. Janjic, U. Blahak and J. Min

contributed to the conceptual design of the research project and A. de Lozar, E. Bauernschubert and K. Stephan contributed to discussion and interpretation of the results.

Competing interests.

345   The authors declare that they have no conflict of interest.

Acknowledgements.   Thanks are given to the DFG (Deutsche Forschungsgemeinschaft) Priority Program 2115:PROM through the project JA 1077/5-1. The work of Y. Feng is sponsored by China Scholarship Council (CSC). T. Janjic is thankful to the DFG for the Heisenberg Award JA 1077/4-1. The work of U. Blahak is supported by the Innovation Programm for applied Research and Development (IAFE) of Deutscher Wetterdienst in the framework of the SINFONY project. Thanks are also given to Roland Potthast from the DWD and Leonhard Scheck from
350   the Hans Ertel Centre for Weather Research (Weissmann et al., 2014; Simmer et al., 2016) at the LMU for technical supports.

Financial support.

    This research has been supported by the DFG and DWD.

References

Aksoy, A., Dowell, D. C., and Snyder, C.: A multiscale comparative assessment of the ensemble Kalman filter for assimilation of radar observations. Part I: Storm-scale analyses, Mon. Wea. Rev., 137, 1805–1824, 2009.

Baldlauf, M., Seifert, A., Förstner, J., Majewski, D., M., R., and Reinhardt, T.: Operational convective-scale numerical weather prediciton with the COSMO model: description and sensitivities, Mon. Wea. Rev., 139, 3887–3905, 2011.

Bick, T., Simmer, C., Trömel, S., Wapler, K., Stephan, K., Blahak, U., Zeng, Y., and Potthast, R.: Assimilation of 3D-Radar Reflectivities with an Ensemble Kalman Filter on the Convective Scale, Quart. J. Roy. Meteor. Soc., 142, 1490–1504, 2016.

Bormann, N., Bonavita, M., Dragani, R., Eresmaa, R., Matricardi, M., and McNally, A.: Enhancing the impact of IASI observations through an updated observation-error covariance matrix, Q.J.R. Meteorol Soc., 142, 1767–1780, 2016.

Caumont, O., Ducrocq, V., Wattrelot, E., Jaubert, G., and Pradier-Vabre, S.: 1D+3DVar assimilation of radar reflectivity data: a proof of concept, Tellus, 62, 173–187, 2010.

Desroziers, G., Berre, L., Chapnik, B., and Poli, P.: Diagnosis of observation, background and analysis-error statistics in observation space, Q. J. R. Meteorol. Soc., 131, 3385–3396, 2005.

Gaspari, G. and Cohn, S. E.: Construction of correlation functions in two and three dimensions, Q. J. R. Meteorol. Soc., 125, 723–757, 1999.

Gastaldo, T., Poli, V., Marsigli, C., Cesari, D., Alberoni, P. P., and Paccagnella, T.: Assimilation of radar reflectivity volumes in a pre-operational framework, Quart. J. Roy. Meteor. Soc, https://doi.org/10.1002/qj.3957, early View, 2021.

Gustafsson, N., Janjić, T., Schraff, C., Leuenberger, D., Weissman, M., Reich, H., Brousseau, P., Montmerle, T., Wattrelot, E., Bucanek, A., Mile, M., Hamdi, R., Lindskog, M., Barkmeijer, J., Dahlbom, M., Macpherson, B., Ballard, S., Inverarity, G., Carley, J., Alexander, C., Dowell, D., Liu, S., Ikuta, Y., and Fujita, T.: Survey of data assimilation methods for convective-scale numerical weather prediction at operational centres, Quart. J. Roy. Meteor. Soc., pp. 1218–1256, 2018.

Hollingsworth, A. and Lonnberg, P.: The statistical structure of short-range forecast errors as determined from radiosonde data. Part 1: the wind field, Tellus, 38, 111–136, 1986.

Hunt, B. R., Kostelich, E. J., and Szunyogh, I.: Efficient data assimilation for Spatiotemporal Chaos: a Local Ensemble Transform Kalman Filter, Physica D: Nonlinear Phenomena, 230, 112–126, 2007.

Janjic, T., Bormann, N., Bocquet, M., Carton, J. A., Cohn, S. E., Dance, S. L., Losa, S. N., Nichols, N. K., Potthast, R., Waller, J. A., and Weston, P.: On the representation error in data assimilation, Quart. J. Roy. Meteor. Soc., 144, 1257–1278, 2018.

Jones, T., Knopfmeier, K., Wheatley, D., Creager, G., Minnis, P., and Palikonda, R.: Storm-scale data assimilation and ensemble forecasting with the NSSL Experimental Warn-on-Forecast System. Part II: Combined radar and satellite data experiments, Wea. Forecasting, 31, 297–327, 2016.

Lange, H. and Janjić, T.: Assimilation of Mode-S EHS Aircraft Observations in COSMO-KENDA, Mon. Wea. Rev., 144, 1697–1711, 2016.

Lange, H., Craig, G. C., and Janjić, T.: Characterizing noise and spurious convection in convective data assimilation, Quart. J. Roy. Meteor. Soc., 143, 3060–3069, 2017.

Lin, Y., Farley, R. D., and Orville, H. D.: Bulk parameterization of the snow field in a cloud model, J. Climate Appl. Meteor., 22, 1065–1092, 1983.

Liu, Z. Q. and Rabier, F.: The interaction between model resolution observation resolution and observation density in data assimilation, Quart. J. Roy. Meteor. Soc, 128, 1367–1386, 2002.

Montmerle, T. and Faccani, C.: Mesoscale assimilation of radial velocities from Doppler radars in a preoperational framework, Mon. Weather
Rev., 137, 1939–1953, 2009.

Raschendorfer, M.: The new turbulence parametrization of LM, COSMO-Newsletter, 1, 89–97, 2001.

Reinhardt, T. and Seifert, A.: A three-category ice scheme for LMK, COSMO News Letter, 6, 115–120, 2006.

Schraff, C., Reich, H., Rhodin, A., Schomburg, A., Stephan, K., Periáñez, A., and Potthast, R.: Kilometre-Scale Ensemble Data Assimilation
for the COSMO Model (KENDA), Quart. J. Roy. Meteor. Soc., 142, 1453–1472, 2016.

Simmer, C., Adrian, G., Jones, S., Wirth, V., Göber, M., Hohenegger, C., Janjić, T., Keller, J., Ohlwein, C., Seifert, A., Trömel, S., Ulbrich,
T., Wapler, K., Weissmann, M., Keller, J., Masbou, M., Meilinger, S., Riβ, N., Schomburg, A., Stein, C., and Vormann, A.: HErZ – The
German Hans-Ertel Centre for Weather Research, Bull. Amer. Meteor. Soc., 97, 1057–1068, 2016.

Simonin, D., Ballard, S., and Li, Z.: Doppler radar radial wind assimilation using an hourly cycling 3D-Var with a 1.5 km resolution version
of the Met Office Unified Model for nowcasting, Q.J.R. Meteorol. Soc., 140, 2298–2314, 2014.

Simonin, D., Waller, J. A., Ballard, S. P., Dance, S. L., and Nichols, N. K.: A pragmatic strategy for implementing spatially correlated
observation errors in an operational system: An application to Doppler radial winds, Quart. J. Roy. Meteor. Soc., 145, 2772–2790, 2019.

Stephan, K., Klink, S., and Schraff, C.: Assimilation of radar-derived rain rates into convective-scale model COSMO-DE at DWD, Quart. J.
Roy. Meteor. Soc., 134, 1315–1326, 2008.

Tiedtke, M.: A comprehensive mass flux scheme for cumulus parameterization in large-scale models, Mon. Wea. Rev., 117, 1779–1799,
1989.

Waller, J. A., Dance, S. L., Lawless, A. S., Nichols, N. K., and Eyre, J. R.: Representativity error for temperature and humidity using the Met
Office high-resolution model, Quart. J. Roy. Meteor. Soc., 140, 1189–1197, 2014.

Waller, J. A., Ballard, S. P., Dance, S. L., Kelly, G., Nichols, N. K., and Simonin, D.: Diagnosing horizontal and inter-channelobservation error
correlations for SEVIRI observations using observation-minus-background and observation-minus-analysis statistics, Remote Sensing,,
8(7), 581, 2016a.

Waller, J. A., Dance, S. L., and Nichols, N. K.: Theoretical insight into diagnosing observation error correlations using observation-minus-
background and observation-minus-analysis statistics, Quart. J. Roy. Meteor. Soc., 142, 418–431, 2016b.

Waller, J. A., Simonin, D., Dance, S. L., Nichols, N. K., and P., B. S.: Diagnosing Observation Error Correlations for Doppler Radar Radial
Winds in the Met Office UKV Model Using Observation-Minus-Background and Observation-Minus-Analysis Statistics, Mon. Wea. Rev.,
144, 3533–3551, 2016c.

Waller, J. A., Bauernschubert, E., Dance, S. L., Nichols, N. K., Potthast, R., and Simonin, D.: Observation Error Statistics for Doppler Radar
Radial Wind Superobservations Assimilated into the DWD COSMO-KENDA System, Mon. Wea. Rev., 147, 3351–3364, 2019.

Wang, Y. and Wang, X.: Direct Assimilation of Radar Reflectivity without Tangent Linear and Adjoint of the Nonlinear Observation Operator
in the GSI-Based EnVar System: Methodology and Experiment with the 8 May 2003 Oklahoma City Tornadic Supercell, Mon. Wea. Rev.,
145, 1447–1471, 2017.

Wattrelot, E., Montmerle, T., and Guerrero, C.: In Proceedings of the seventh European conference on radar in meteorology and hydrology,
www.meteo.fr/cic/meetings/2012/ERAD/extended_abs/NWP_401_ext_abs.pdf, 2012.

Wedi, N. P.: Increasing horizontal resolution in numerical weather prediction and climate simulations: illusion or panacea?, Phil. Trans. R.
Soc., 372, 20130 289, 2014.

425 Weissmann, M., Göber, M., Hohenegger, C., Janjić, T., Keller, J., Ohlwein, C., Seifert, A., Trömel, S., Ulbrich, T., Wapler, K., Bollmeyer, C., and Deneke, H.: Initial phase of the Hans-Ertel Centre for Weather Research - A virtual centre at the interface of basic and applied weather and climate research, Meteorologische Zeitschrift, 23, 193–208, 2014.

Werner, M.: In Proceedings of the eighth European conference on radar in meteorology and hydrology, Garmisch-Partenkirchen, Germany, http://www.pa.op.dlr.de/erad2014/programme/ExtendedAbstracts/079_Werner.pdf, 2014.

430 Weston, P. P., Bell, W., and Eyre, J. R.: Accounting for correlated error in the assimilation of high-resolution sounder data., Quart. J. Roy. Meteor. Soc., 140, 2420–2429, 2014.

Zängl, G., Reinert, D., Rípodas, P., and Baldauf, M.: The ICON (ICOsahedral Non-hydrostatic) modelling framework of DWD and MPI-M: Description of the non-hydrostatic dynamical core, Quart. J. Roy. Meteor. Soc., 141, 563–579, 2015.

Zeng, Y.: Efficient Radar Forward Operator for Operational Data Assimilation within the COSMO-model, PhD dissertation, Karlsruhe
435 Insititute of Technology, 2013.

Zeng, Y., Blahak, U., Neuper, M., and Jerger, D.: Radar Beam Tracing Methods Based on Atmospheric Refractive Index, J. Atmos. Ocean. Tech, 31, 2650–2670, 2014.

Zeng, Y., Blahak, U., and Jerger, D.: An efficient modular volume-scanning radar forward operator for NWP models: description and coupling to the COSMO model, Quart. J. Roy. Meteor. Soc., 142, 3234–3256, 2016.

440 Zeng, Y., Janjić, T., de Lozar, A., Blahak, U., Reich, H., Keil, C., and Seifert, A.: Representation of model error in convective-scale data assimilation: additive noise, relaxation methods and combinations, J. Adv. Model. Earth Syst., 10, 2889–2911, 2018.

Zeng, Y., Janjić, T., Sommer, M., de Lozar, A., Blahak, U., and Seifert, A.: Representation of model error in convective-scale data assimilation: additive noise based on model truncation error, J. Adv. Model. Earth Syst., 11, 752–770, 2019.

Zeng, Y., Janjić, T., de Lozar, A., Rasp, S., Blahak, U., Seifert, A., and Craig, G. C.: Comparison of methods accounting for subgrid-scale
445 model error in convective-scale data assimilation, Mon. Wea. Rev., 148, 2457–2477, 2020.

Zeng, Y., Janjic, T., de Lozar, A., Welzbacher, C. A., Blahak, U., and Seifert, A.: Assimilating radar radial wind and reflectivity data in an idealized setup of the COSMO-KENDA system, Atmos. Res., 249, 105 282, 2021a.

Zeng, Y., de Lozar, A., Janjić, T., and Seifert, A.: Applying a new integrated mass-flux adjustment filter in rapid update cycling of convective-scale data assimilation for the COSMO-model (v5.07), Geosci. Model Dev., 14, 1295–1307, 2021b.

450 Zhang, F., Snyder, C., and Sun, J.: Impacts of initial estimate and observation availability on convective-scale data assimilation with an ensemble Kalman filter, Mon. Wea. Rev., 132(5), 1238–1253, 2004.